

pubs.acs.org/JPCC Article

# Probing Chemical Vapor Deposition Growth Mechanism of Polycrystalline MoSe<sub>2</sub> by Near-Field Photoluminescence

Published as part of The Journal of Physical Chemistry virtual special issue "Nanophotonics for Chemical Imaging and Spectroscopy".

Sharad Ambardar, Hana N. Hrim, Chenwei Tang, Shuai Jia, Weibing Chen, Jun Lou, and Dmitri V. Voronine\*

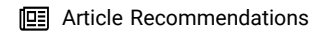


Cite This: J. Phys. Chem. C 2022, 126, 13821–13829



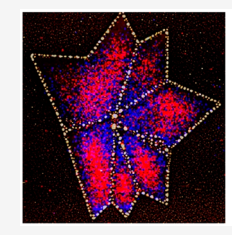
**ACCESS** I

III Metrics & More



S Supporting Information

ABSTRACT: Chemical vapor deposition (CVD) growth of atomically thin 2D materials, such as transition metal dichalcogenides (TMDs), is a complex process that has not been completely understood. Large-scale growth of monolayer TMDs often leads to polycrystalline films with heterogeneous morphological and optical properties. Previous optical studies of 2D materials by far-field photoluminescence (PL) provided insights into CVD growth mechanisms of simple crystals, which were, however, limited in spatial resolution due to the diffraction limit. Here we performed correlated morphological and tip-enhanced PL (TEPL) imaging of CVD-grown polycrystalline monolayer molybdenum diselenide (MoSe<sub>2</sub>) flakes with heterogeneous optical response. We observed nanoscale





spatial variations of the optical band gap due to growth-induced thermal strain, revealing the different roles of aligned particles (APs) at crystal edges and grain boundaries (GBs) in thermal strain relaxation. TEPL imaging showed the strain-free near-field PL at GBs, revealing the direct connection between MoSe<sub>2</sub> and APs. These results may be used to improve nanoscale bandgap engineering techniques and CVD growth scalability, leading to optimized crystal growth and high performance optoelectronic nanodevices.

### INTRODUCTION

The reduced dimensionality of 2D materials leads to distinct properties compared to bulk. Monolayer transition metal dichalcogenides (TMDs) exhibit direct band gaps for applications in optoelectronic devices, for example, light emitting diodes, single photon emitters, sensing, and solar cells. Monolayer MoS<sub>2</sub> is the most widely studied TMD. MoSe<sub>2</sub> may have advantages due to its narrower band gap, narrower line width, and tunable excitonic properties. In, 12

The bright photoluminescence (PL) in TMDs can be controlled by applied strain. 13-15 CVD-grown TMD crystals often have a native nonuniform strain as a result of different thermal expansion coefficients compared to the substrate. 16 Previous studies of strain and structure heterogeneity provided insights into CVD growth mechanisms. 16,17 Earlier morphological studies revealed two kinds of nanoparticles that played a role in the CVD growth, namely, the randomly dispersed random particles (RPs), and the aligned particles (APs) at the crystal edges.<sup>17</sup> They proposed a 3-step mechanism of MoSe<sub>2</sub> CVD growth which included (i) reduction and evaporation of MoO<sub>3</sub> and Se; (ii) formation of RPs with MoO<sub>x</sub>Se<sub>v</sub> composition (0.22 < x < 1.25 and 0.13 < y < 0.5); (iii) selenization of the RPs by the vapor-phase Se to form MoSe<sub>2</sub> and APs with  $MoO_z$  composition (z > 1.5 and trace amounts of Se) as reaction byproducts. 17 RPs were shown to be the inplane feedstock sources of Mo. APs were shown to contain the oxygen expelled from  $MoSe_2$  edges in the form of  $MoO_z$  nanoscale agglomerates. This solid—vapor reaction was shown to be reversible at the edges, and the detachment of the APs from the edges was related to crystal quality. However, the role of the APs at the grain boundaries (GBs) of polycrystalline flakes was not thoroughly investigated. The crystal growth at the GBs is slower than at the edges due to the slower in-plane reactant diffusion rates from the surrounding RPs toward the nucleation center. The detachment of the APs from  $MoSe_2$  in the GB areas may affect the optical properties of the polycrystalline samples. Understanding the nanoscale morphology and optical properties of the GBs requires high resolution near-field characterization techniques.

To achieve a more accurate spectroscopic characterization, higher spatial resolution than that provided by the conventional confocal PL is needed. Mapping local band gap variation is essential for fabricating optoelectronic devices. However, confocal microscopy is restricted by the diffraction limit, and

Received: May 31, 2022 Revised: July 21, 2022 Published: August 3, 2022





therefore, is insufficient. Near-field imaging techniques, <sup>20–35</sup> such as TEPL imaging, are required for accurate band gap characterization. In TEPL imaging, a plasmonic scanning probe tip is used for increasing the spatial resolution of the PL signals. By focusing the excitation laser beam on the plasmonic tip, localized plasmons can be generated at the tip apex. <sup>36–38</sup> The strong near fields generated by the surface plasmons interact with the sample and enhance the PL signals providing high spatial resolution imaging.

Here, we performed TEPL measurements of CVD-grown monolayer polycrystalline  $MoSe_2$  with nanoscale spatial resolution, providing an improved characterization of the band gap correlated with the morphology compared with the conventional far-field imaging. We observed heterogeneous distribution of the PL shifts at the crystal edges and GBs, indicating the role of APs in CVD growth and strain relaxation. Our results may be used to better understand the local properties of 2D materials and to improve optoelectronic devices.

#### EXPERIMENTAL METHODS

**Synthesis.** Monolayer  $MoSe_2$  was synthesized in a homebuilt CVD furnace. <sup>17</sup>  $MoO_3$  and Se powders (Sigma- Aldrich), used as Mo and Se sources, were placed in the center and the upstream location of the furnace, respectively. Clean  $SiO_2/Si$  substrates facing the  $MoO_3$  source were placed in the furnace center. Typically, when the furnace temperature ramps to 750 °C, after 15 min purging,  $MoO_3$  evaporates and reacts with the flowing Se carried by  $H_2$  gas ( $\sim$ 50 sccm), forming monolayer  $MoSe_2$  on the  $SiO_2/Si$  substrate. After 10 min growth, the furnace was naturally cooled down to room temperature.

**Characterization.** Confocal Raman and PL spectroscopies were used to characterize the monolayer MoSe<sub>2</sub> by Raman peak position and Raman/PL intensity ratio. The experiments were carried out using the LabRAM Raman microscope (Horiba Scientific).

Correlated Atomic Force Microscopy (AFM) and Tip-Enhanced Photoluminescence (TEPL). AFM and TEPL measurements were carried out using the state-of-the-art commercial system (OmegaScopeTM 1000, coupled with LabRAM Evolution spectrometer, Horiba Scientific). Silicon tips were used for AFM, and Au-coated tips with apex radius ~20 nm were used for TEPL measurements. The 660 nm laser was focused using objective lens (NA = 0.9) on the tip apex, and the sample was scanned while recording at each point both the near-field (NF) and the far-field (FF) PL signals with a tip-sample distance of ~0.3 nm and ~20 nm, respectively. AFM and FF PL measurements were performed in the tapping mode with a 20 nm average tip-sample distance (TSD). NF TEPL imaging was performed in the contact mode. We separated the NF and FF signals by subtracting the tip-out (TSD = 20 nm) from the tip-in (TSD = 0.36 nm) signals. The subtracted maps are pure NF maps and do not contain any FF contribution. Using backscattering configuration with a 659.38 nm edge filter, the scattered signal was collected and detected by spectrometer with 600 g/mm grating coupled to a CCD camera. The PL signal was collected by the illumination objective. The angle between the incident laser optical axis and the horizontal sample plane was 25°. The angle between the tip and the sample plane was 78°. The incident light polarization was along the tip axis. The tip and the laser were stationary during the experiments, while the sample stage was scanned. The localized surface plasmons of the tip enhance

the electromagnetic field, leading to the enhanced PL emission. The laser power was 1 mW and the step size of the scan was 67 nm, with 0.2 s acquisition time. The detailed setup for the TEPL experiments was previously described.<sup>23</sup>

#### RESULTS AND DISCUSSION

The schematic of the experimental setup in Figure 1 shows a single monolayer  $MoSe_2$  crystal on the  $SiO_2/Si$  substrate

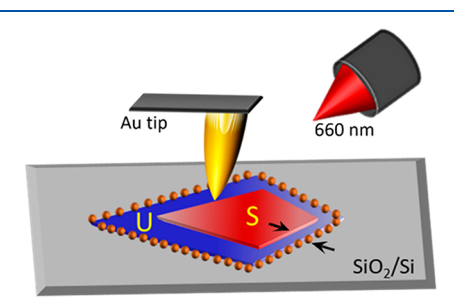


Figure 1. Schematic of the experimental setup for the correlated AFM and TEPL imaging of MoSe<sub>2</sub> crystals. The unstrained (U) edge and strained (S) center of the crystal emit PL signals of different energies. The crystal edges are decorated by the aligned particles (APs). The near-field PL signal is generated by focusing the 660 nm laser at the apex of the Au-coated tip. The unstrained (blue) perimeter width is indicated by arrows.

grown using the CVD method described above. The crystal edges are decorated by APs. The PL signals from the unstrained (U) edge of the crystal are shown in blue, while the PL of the strained (S) center region is red. The 660 nm laser was focused at the apex of the Au tip. The TEPL signal was collected with the same microscope objective that was used for excitation. We define the perimeter width of the unstrained (blue) edge as the full width half-maximum (fwhm) of the line profile perpendicular to the crystal edge as shown by arrows in Figure 1. Polycrystalline flakes have a single or multiple nucleation centers in a common location, forming flower-like morphologies. The adjacent MoSe<sub>2</sub> crystals form GBs which are also decorated with APs. The APs at crystal edges and at GBs may have different properties and functions.

Figures 2 and 3 show the morphology and PL imaging of polycrystalline monolayer  $MoSe_2$  flakes (referred to as flakes 1 and 2 in the following). Flake 1 consists of seven merged crystals with straight edges labeled 1'-7'. The AFM height image in Figure 2a confirms the monolayer thickness of <1 nm. It also shows the presence of APs at the edges and at the GBs between the crystals. AFM was used to determine  $\sim 16$  nm average height of the APs at the edges, and  $\sim 10$  nm average height of the APs in the GB regions (see the corresponding discussion in what follows).

Normalized FF (Figure 2b) and NF (Figure 2c) PL spectra from the center (red line) and edge (blue line) areas of crystal 7′ (highlighted by red and blue boxes in Figure 2h) indicate ~10 meV shift of the FF and NF peak positions,  $\Delta_{FF}$  and  $\Delta_{NF}$ , respectively. This spectral shift is attributed to thermal strain as discussed below. The similarity between the FF and NF spectral profiles indicates the absence of local tip-induced strain effects. For comparison, we also show the total PL signals integrated over the whole flake in both normalized FF and NF signals (Figure 2d).

We used NF imaging to investigate the spatial distribution of the PL signals. Figure 2e-h and Figure 2i-l show the maps of

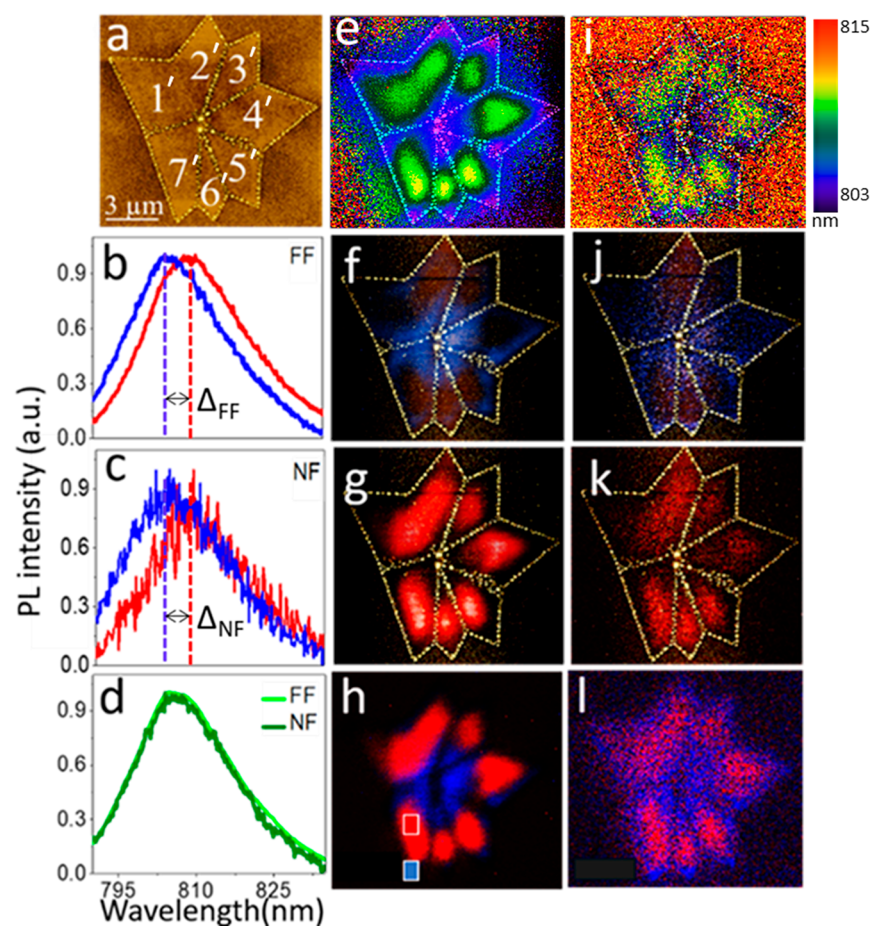


Figure 2. Morphology and PL imaging of polycrystalline MoSe<sub>2</sub> (flake 1) with straight edges. (a) AFM height image with individual crystals labeled 1'-7'. (b) Normalized far-field (FF) PL spectra and (c) normalized near-filed (NF) PL spectra from the center and edge of crystal 7' shown by highlighted red and blue boxes in panel h. (d) Normalized FF and NF spectra averaged over the whole flake corresponding to FF (e) and NF (i) PL wavelength maps. FF (f,g,h) and NF (j,k,l) PL maps obtained by Gaussian fitting of the edge (blue) and center (red) areas, overlapped with AFM images.

integrated FF and NF PL signals, respectively. The FF (Figure 2e) and NF (Figure 2i) PL wavelength maps integrated show the strain-induced PL red shift starting at the crystal edges toward the crystal center areas. The NF and FF PL maps were obtained with the spatial resolution of ~80 nm and ~480 nm, respectively, as shown in the Supporting Information Figure S1b and S 1d, respectively. Due to the higher resolution, the NF map in Figure 2i provides a more detailed picture of the heterogeneous PL distribution compared to the FF map in Figure 2e. It shows more clearly the decrease of the PL signal in the GB regions between the crystals. We performed Gaussian fitting of the PL spectra and plotted the integrated intensities of the separated spectral components that correspond to the unshifted (blue) PL of the crystal edges (Figure 2f,j) and the red-shifted (red) PL of the crystal center areas (Figure 2g,k). We also plotted their overlapped maps in Figure 2h,l. All PL maps in Figure 2 except maps h and l were overlapped with the AFM height images to correlate the flake morphology with the optical response. Interestingly, the unshifted PL maps in Figure 2f,j show the predominant PL signals both at the flake edges and at the flake center. Furthermore, the central part of the flake has a stronger unshifted PL compared to the edges. Moreover, the uneven, heterogeneous width of the unshifted PL perimeter was observed over the whole flake area. Note that the low intensity

brown color in Figure 2f,j is due to the spatial overlap of the unstrained PL with the AFM images. It does not indicate any presence of the strained PL.

Figure 3 shows the morphology and PL imaging of a polycrystalline monolayer  $MoSe_2$  flake (referred to as flake 2 below). It consists of 12 merged crystals labeled 1–12 with curved edges, decorated with APs at the edges and at the GBs. The edge curvature was previously attributed to the edge termination properties.<sup>39,40</sup>

Normalized FF (Figure 3b) and NF (Figure 3c) PL spectra from the center (red line) and edge (blue line) areas of crystal 12 (highlighted by red and blue boxes in Figure 3h) indicate the FF and NF spectral shifts of  $\Delta_{\rm FF}\sim 10$  meV and  $\Delta_{\rm NF}\sim 15$  meV, respectively. This difference between the FF and NF spectral shifts is attributed to the combination of the thermal strain, as discussed above, and an additional local tip-induced strain due to the tip–sample interaction. For comparison, we also show the total PL signals integrated over the whole flake (Figure 3d). However, the total PL does not clearly show the tip-induced spectral peak shift due to the relatively small NF intensity compared to the FF signal. The smaller size and curved edges of flake 2 allow for a larger contribution of the tip–sample interaction to the NF PL.

The observed PL red shift at the center of the MoSe<sub>2</sub> crystals is caused by tensile strain due to the difference in thermal

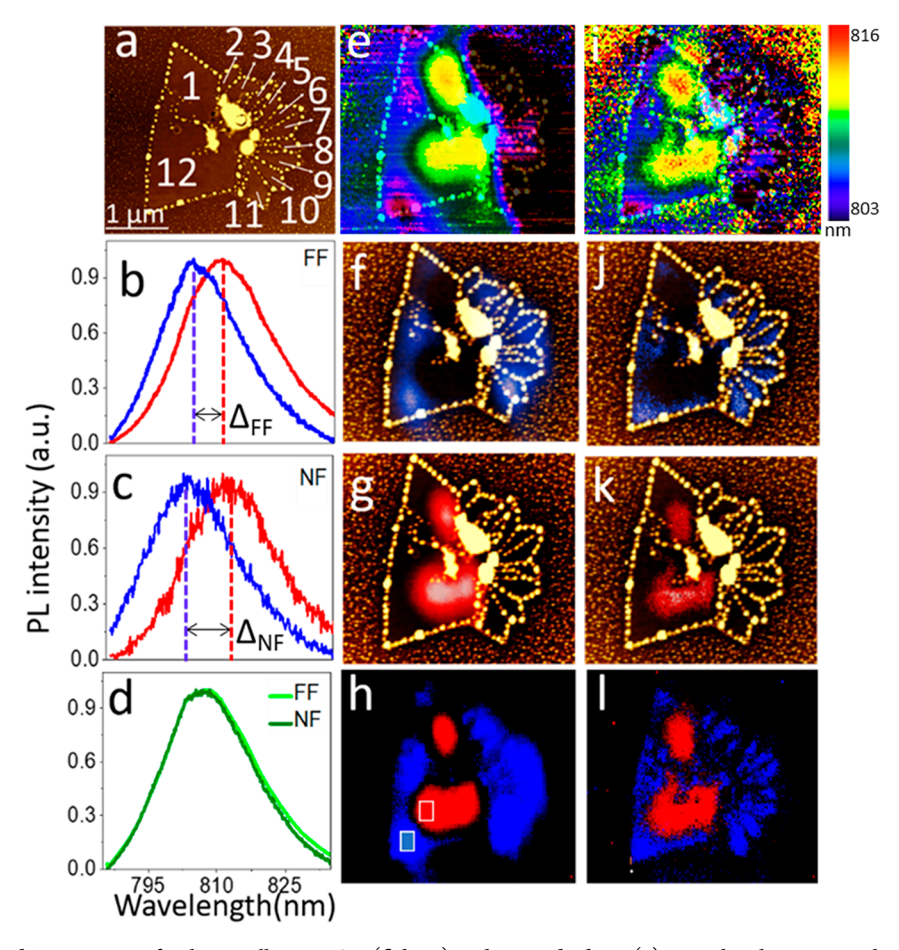


Figure 3. Morphology and PL imaging of polycrystalline MoSe<sub>2</sub> (flake 2) with curved edges. (a) AFM height image with individual crystals labeled 1–12. (b) Normalized far-field (FF) PL spectra and (c) normalized near-field (NF) PL spectra from the center and edge of crystal 12 shown by highlighted red and blue boxes in panel h. (d) Normalized FF and NF spectra averaged over the whole flake corresponding to FF (e) and NF (i) PL wavelength maps. FF (f,g,h) and NF (j,k,l) PL maps obtained by Gaussian fitting of the edge (blue) and center (red) areas, overlapped with AFM images.

expansion coefficients of  $MoSe_2$  and the supporting  $SiO_2$  substrate. Similar thermal strain was previously observed in CVD-grown  $MoS_2$ . We estimated the thermal strain using the previously reported temperature dependence of the thermal expansion coefficient of  $MoSe_2^{\ 43}$ 

$$a = 3.3 + 0.24 \times 10^{-4} t + 0.012 \times 10^{-7} t^2$$
 (1)

using the temperature (t) during CVD growth (750 °C) and the room temperature (23 °C):

$$\epsilon = \frac{a(750 \,^{\circ}\text{C}) - \alpha(23 \,^{\circ}\text{C})}{\alpha(23 \,^{\circ}\text{C})} = 0.54\%$$

which agrees with the experimental PL spectral shift.

The FF PL imaging was not able to resolve the individual crystals 2–11, which appear as one blurred area in Figure 3e,f,h. On the other hand, the high spatial resolution of NF PL allowed for resolving individual crystals in Figure 3i,j,l. The NF PL images fit well into the AP-decorated outlines of the individual crystals in Figure 3j. Figure 3g,k show the absence of strain in the FF and NF PL images of small crystals 2–11. Large crystals 1 and 12 show regions of strain in the center areas.

Figure 4 shows how the unstrained and strained NF PL signals correlate with the AP topography at the crystal edges using line profiles. The unstrained (blue) and strained (red)

NF PL images in Figure 4a and 4e, respectively, show uneven, heterogeneous distributions, with the predominant strained PL at the crystal center. Figure 4i shows the overlap of both strained and unstrained NF PL maps with the AFM height image showing APs at the edges. Figure 4a shows three dashed lines that correspond to the line profiles in Figure 4 panels b-d and f-h, that are approximately perpendicular to the edges. The NF PL signals were obtained by subtracting the tip-out from the tip-in PL signals. The tip-out signals contain only the FF PL, while the tip-in signals contain both FF and NF PL contributions. Line profiles 1-3 were obtained for the varying distance between the APs at the opposite crystal edges. The distance between the APs in profile 1 is larger than the average size of the strain-free perimeter and contains both strained and unstrained PL signals. Both PL signals vanish at the AP positions in Figure 4b,f, which indicates the absence of MoSe<sub>2</sub> and the detachment of the APs from the edges. Interestingly, the unstrained PL signal in the middle of the profile in Figure 4b shows negative values, which correspond to the maximum of the strained PL profile in Figure 4f. This indicates the effect of the tip in NF PL imaging by the tip-induced local strain. Negative NF values mean that the unstrained tip-in PL signal is smaller than the tip-out signal, and the tip affects the MoSe<sub>2</sub> optical response. However, the tip-induced effect is only  $\sim 10\%$ of the total PL intensity and does not obscure the results of imaging the native thermal strain. Profile 3 corresponds to the

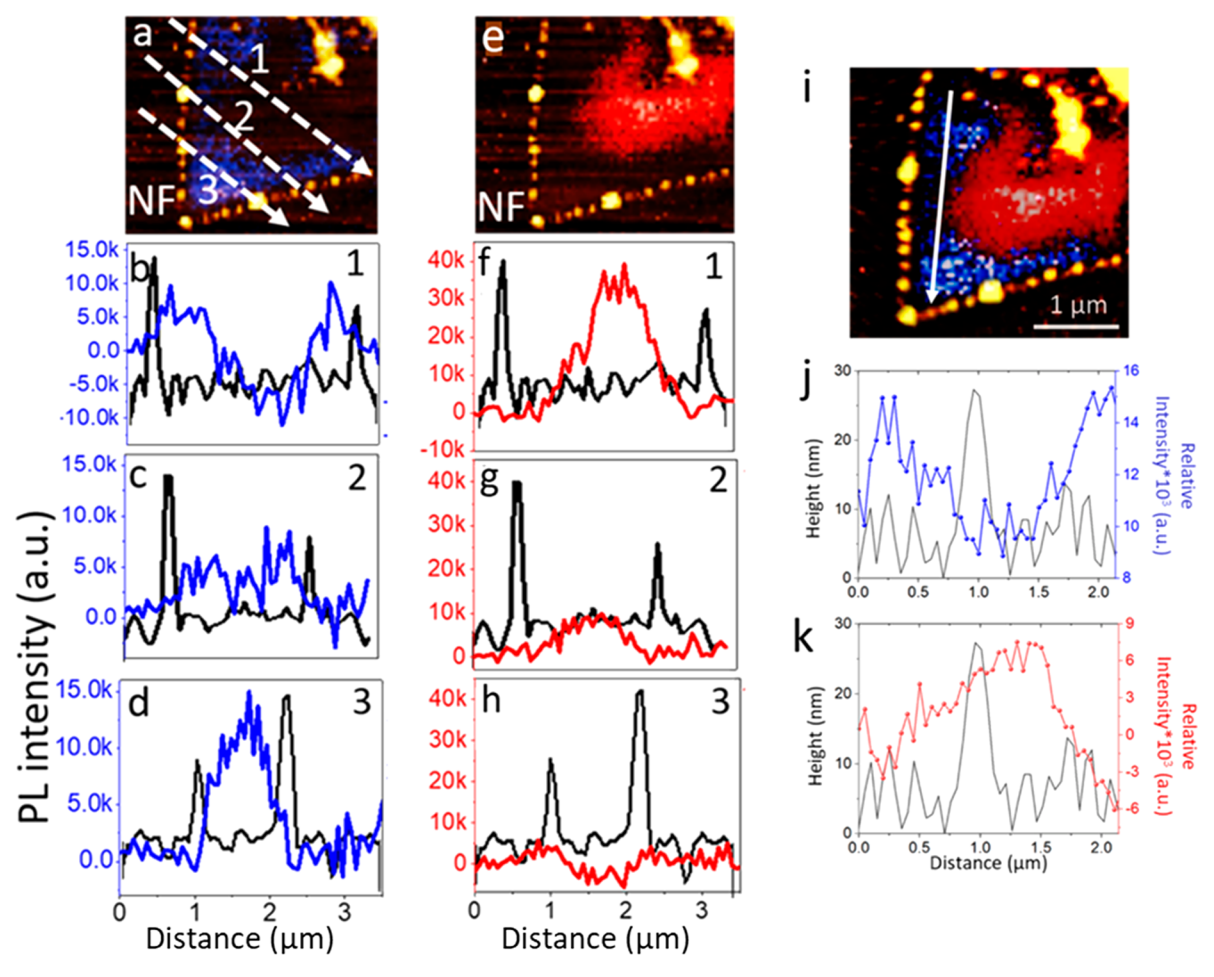


Figure 4. Correlated topographic (AFM) and optical (NF PL) line profiles across MoSe<sub>2</sub> crystal 12 of flake 2. Separated unstrained (a), strained (e), and combined (i) NF PL images overlapped with AFM height maps. Dashed and solid arrows in panels a and i indicate positions of line profiles perpendicular and parallel to the crystal edges, respectively, in the unstrained (b-d, j) and strained (f-h, k) PL signals.

distance between the APs of less than 1  $\mu$ m, where the unstrained PL is dominant. Similar profiles are shown for smaller crystals with an interparticle distance of 0.6  $\mu$ m (Figure S2a -d) and 1  $\mu$ m (Figure S2e-h). They demonstrate the advantage of high-resolution NF PL imaging that is able to resolve nanoscale local strain variations. In contrast, the corresponding FF PL imaging cannot provide the same level of precision in the correlation between the topography and optical response. Figure S3 shows the correlated AFM and FF PL line profiles across MoSe<sub>2</sub> crystal 12 of flake 2. Contrary to Figure 4, Figure S3 presents incorrect and misleading information, showing nonzero unstrained and strained FF PL signals at the positions of the APs at the crystal edges. On the other hand, the corresponding NF PL maps and profiles in Figure 4 show the absence of the PL signal at the APs, indicating that the APs are not directly connected to the crystal edges. The FF PL fails to provide this information, which is directly relevant to the mechanistic understanding of the CVD growth mechanism.

Figure 4 panels j and k show AFM and NF PL line profiles parallel to the MoSe<sub>2</sub> crystal edge, which correspond to the white arrow in Figure 4i, while the AFM height profiles correspond to the APs on the left of the white arrow. The strained and unstrained PL signals show anticorrelated behavior with the minimum strain-free perimeter corresponding to the largest AP height and the maximum strained PL.

This correlation between the AP height and strain indicates the role of APs in optical properties of MoSe<sub>2</sub> crystals.

Next we investigated the properties of APs at GBs and their role in MoSe<sub>2</sub> PL. Figure 5 panels a and i show the AFM height images of crystal 7' of flake 1 and crystals 10 and 11 of flake 2, respectively, highlighting APs at the crystal edges (referred to as APEs for distinction) and APs at GBs (referred to as APGs). The average height and width of the APEs and APGs for both flakes show that APGs are smaller than APEs (Figure 5d,j). Overlapped AFM and NF PL images of the unstrained (blue) and strained (red) PL signals in Figure 5b show the presence of PL signals at the GBs (see also the zoomed-in GB region in Figure 5c). This shows that the APGs are not detached from the adjacent MoSe2 crystals in the GB regions. The spatial resolution of TEPL is 80 nm as shown in Figure S1, which is smaller than the average APE or APG width. Therefore, scanning the GB area with the plasmonic tip generates a continuous NF PL map with 80 nm resolution, providing evidence of the preserved direct contact between the APGs and MoSe<sub>2</sub> crystals. This is different from the previously considered CVD growth mechanism without any direct contact between the APs and edges, where the APs were detached from the MoSe<sub>2</sub> crystals. <sup>17</sup> The slower growth rate at GBs compared to the crystal edges may explain the smaller size of APGs compared to APEs.

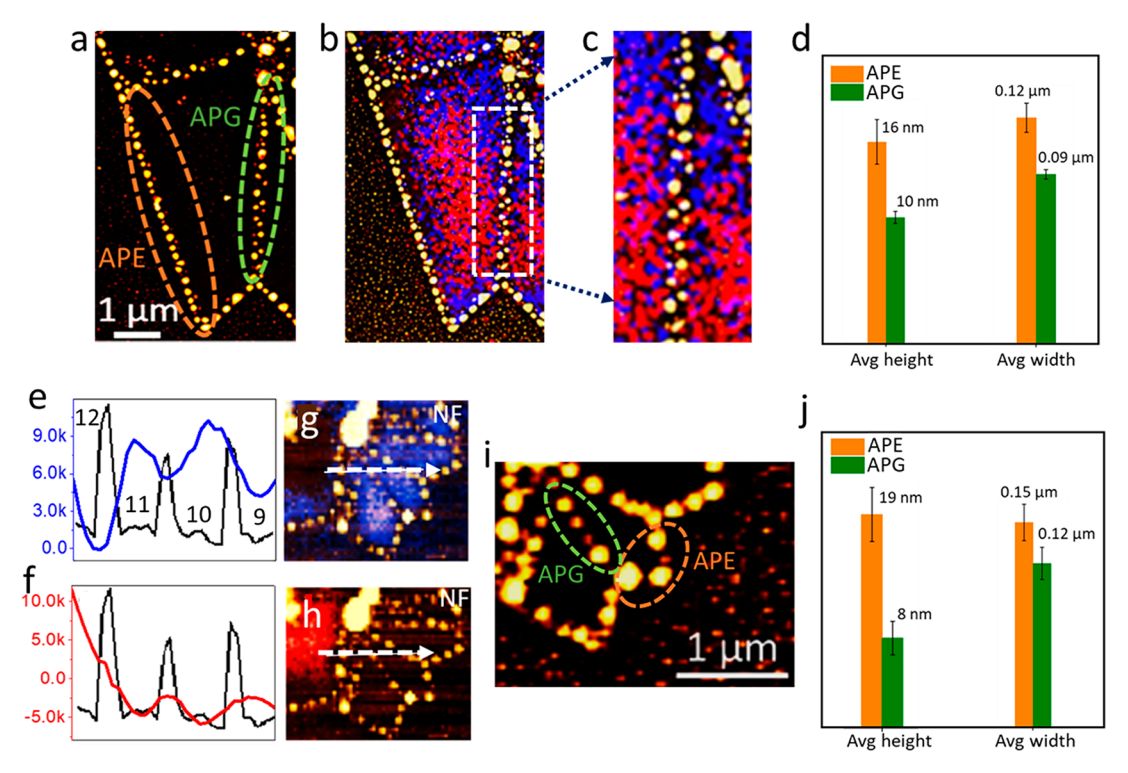


Figure 5. Correlated AFM and NF PL imaging of APs at the crystal edges (APEs) and APs at GBs (APGs). AFM height images of crystal 7' of flake 1 (a) and crystals 10–11 of flake 2 (i) show the comparison between the average height and width of APEs and APGs d and j, respectively. (b) Overlapped AFM and NF PL images of the unstrained (blue) and strained (red) signals. (c) Zoomed-in GB region. Correlated AFM height and NF unstrained (e) and strained (f) PL profiles that correspond to the dashed arrows in the NF PL maps g and h, respectively.

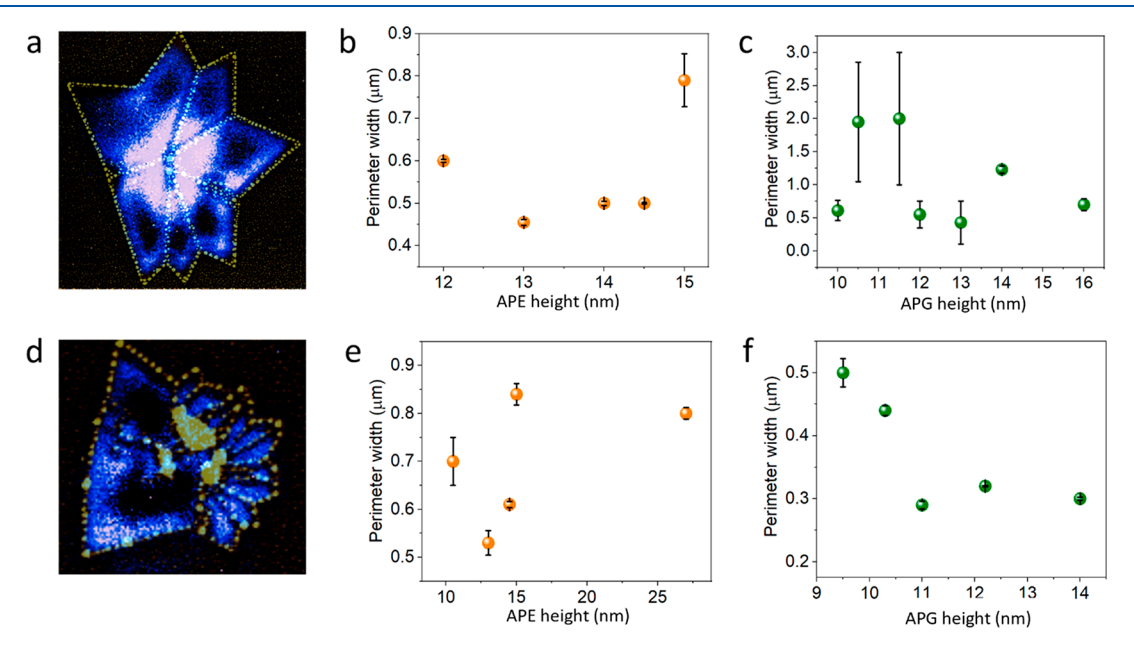


Figure 6. Dependence of the strain-free perimeter width on the APE and APG height for polycrystalline  $MoSe_2$  flakes with straight (a-c) and curved (d-f) edges.

Figure 5g,h show the unstrained and strained NF PL maps, respectively, of crystals 10 and 11 of flake 2 overlapped with AFM height image. The line profiles that correspond to dashed arrows are shown in Figure 5e,f. These results are in agreement with the corresponding maps for flake 1 shown above and support the conclusion that the APGs are smaller than APEs, and they preserve the unstrained PL signals. For example, Figure 5e shows significant NF PL signals on top of the middle

and right APGs between crystals 11–10 and 10–9, respectively. The corresponding strained NF PL signals in Figure 5f show the opposite behavior compared to the unstrained PL. In contrast, the corresponding FF PL signals in Figure S4 provide different and misleading information due to the lower resolution. For example, the unstrained (blue) and strained (red) FF PL profiles in Figure S4d,f, respectively, do not show any significant correlation with the AFM height

profiles (black lines in these figures). The APG between crystals 11 and 10 show both unstrained and strained FF PL signals due to the mixed contributions of the surrounding areas. These results highlight the significant advantages of the NF versus FF PL signals that are relevant to the mechanistic understanding of optical properties of CVD-grown 2D materials. The possible drawbacks of TEPL are weaker NF PL signals compared to the FF PL (Figure S5). Despite this, our results showed good signal-to-noise levels.

Figure 6 shows the dependence of the strain-free perimeter width on the APE and APG height for polycrystalline MoSe<sub>2</sub> flakes with straight (Figure 6a-c) and curved (Figure 6d-f) edges. We obtained the average of the perimeter width of the unstrained (blue) edge as the full width half-maximum (fwhm) of the average line profile perpendicular to the crystal edge as shown by arrows in Figure 1. We used several (5-10) line profiles at different locations along each crystal edge. The intensity scale of the unstrained NF PL maps in Figure 6a,d was adjusted to highlight the differences between the APE and APG areas. Figure 6a shows stronger PL signal in the APG areas close to the center of flake 1 with straight edges. On the other hand, a different behavior was observed in Figure 6d for flake 2 with curved edges, where the strain-free PL was weaker at the flake center close to the APG areas compared to the APEs. This indicates different growth kinetics and strain relaxation related to edge shape.

Previous studies of the strain-free perimeter of CVD-grown MoS<sub>2</sub> showed the difference between the PL of crystals with straight and curved edges.<sup>39</sup> The curved edges showed a larger FF PL strain-free perimeter that was related to different edge termination. However, the CVD growth mechanism was different, and no APs were involved. No strain-free PL was observed at GBs. Here, our NF PL signals have higher spatial resolution compared to the FF PL. We observed larger absolute values and larger variations of the strain-free perimeter at the APGs compared to APEs for crystals with straight edges (Figure 6b,c). On the other hand, we observed smaller values and smaller variations of the perimeter at the APGs compared to APEs for crystals with curved edges (Figure 6e,f).

The difference between the strain-free perimeter width of APGs varies significantly because the in-plane material diffusion rate from outside of the crystals toward GBs decreases with the increase of the crystal size. On the other hand, the diffusion rate toward crystal edges stays constant during the whole CVD growth. Therefore, the strain-free perimeter of APEs does not vary much. The smaller perimeter width of APGs of flake 2 is attributed to the smaller size of flake 2 crystals 1–12 compared to the larger size of flake 1 crystals 1′-7′. No significant correlation between the perimeter width and AP width was observed.

Based on these results we propose that APs play an important role in strain relaxation in GB areas of polycrystal-line MoSe<sub>2</sub> flakes. Our experiments showed that the APs are detached from MoSe<sub>2</sub> at the flake outer edges. However, they are attached at GBs. This attachment may play a role in the reversible growth reaction at the end of the CVD growth period, especially, during the cooling stage, when the thermal strain is induced.

The direct contact between MoSe<sub>2</sub> and GBs is further supported by the increased strained NF PL line profiles in Figure 5f at the positions of GBs. This indicates the effect of the tip in NF PL imaging of MoSe<sub>2</sub> by the tip-induced local

strain while placing the tip on APG. Since the  $MoSe_2$  and GB are connected, the force of  $\sim 50-100$  nN on APG by the tip affects the PL signal of  $MoSe_2$ . Also, another effect, namely, the increase of the tip- $MoSe_2$  distance when the tip is on top of APG, leads to a slight decrease of the unstrained NF PL signals on top of APGs in Figure 5e.

### CONCLUSIONS

Our results indicate higher crystal quality at the center of the flakes compared to flake edges based on the overall NF PL distribution and on connections between APs and crystal edges. Figures 2i and 3i show more homogeneous NF PL patterns in the centers. For example, crystal 1 of both flakes 1 and 2 has a significantly smaller PL intensity compared to other crystals. The intensities of small crystals of flake 2 vary. The connection between the APs and crystal edges was previously related to crystal quality, where the connected crystals were shown to be of higher quality. 17 Here we showed that the connection between MoSe2 and APGs is correlated with the size of the strain-free perimeter. The crystals with straight edges had a larger perimeter at the GBs and possibly higher quality, that is, a smaller number of defects. Straight and curved edge morphologies were previously attributed to Mo zigzag (Mo-zz) and S zigzag (S-zz) edge termination in MoS<sub>2</sub>.<sup>39,40</sup> We expect similar behavior in MoSe<sub>2</sub>. The previous three-step model ab initio simulations were performed using the Se-zz edges. Our observed differences in the NF PL properties of these crystals suggest possible modifications of the growth mechanism at the Mo-zz edge.

## ASSOCIATED CONTENT

## Supporting Information

The Supporting Information is available free of charge at https://pubs.acs.org/doi/10.1021/acs.jpcc.2c03728.

Five figures with captions showing the spatial resolution and additional supporting images and spectra (PDF)

## AUTHOR INFORMATION

## **Corresponding Author**

Dmitri V. Voronine — Department of Medical Engineering and Department of Physics, University of South Florida, Tampa, Florida 33620, United States; orcid.org/0000-0002-8841-7657; Email: dmitri.voronine@gmail.com

## Authors

Sharad Ambardar — Department of Medical Engineering, University of South Florida, Tampa, Florida 33620, United States

Hana N. Hrim – Department of Physics, University of South Florida, Tampa, Florida 33620, United States

Chenwei Tang – Institute for Quantum Science and Engineering, Texas A&M University, College Station, Texas 77843, United States

Shuai Jia — Department of Materials Science & Nano Engineering, Rice University, Houston, Texas 77005, United States

Weibing Chen – Department of Materials Science & Nano Engineering, Rice University, Houston, Texas 77005, United States

Jun Lou – Department of Materials Science & Nano Engineering and Department of Chemistry, Rice University, Houston, Texas 77005, United States; oorcid.org/0000-0002-4351-9561

Complete contact information is available at: https://pubs.acs.org/10.1021/acs.jpcc.2c03728

#### Notes

The authors declare no competing financial interest.

### ACKNOWLEDGMENTS

S.J., W.C., and J.L. gratefully thank the support by the Welch Foundation (Grant C-1716) and the National Science Foundation ATOMIC center (EEC-2113882).

## REFERENCES

- (1) Wang, Q. H.; Kalantar-Zadeh, K.; Kis, A.; Coleman, J. N.; Strano, M. S. Electronics and Optoelectronics of Two-Dimensional Transition Metal Dichalcogenides. *Nature Nanotechnol.* **2012**, *7* (11), 699–712
- (2) Ross, J. S.; Klement, P.; Jones, A. M.; Ghimire, N. J.; Yan, J.; Mandrus, D. G.; Taniguchi, T.; Watanabe, K.; Kitamura, K.; Yao, W.; et al. Electrically Tunable Excitonic Light-Emitting Diodes Based on Monolayer WSe 2 p—n Junctions. *Nature Nanotechnol.* **2014**, 9 (4), 268–272.
- (3) Baugher, B. W.; Churchill, H. O.; Yang, Y.; Jarillo-Herrero, P. Optoelectronic Devices Based on Electrically Tunable p—n Diodes in a Monolayer Dichalcogenide. *Nature Nanotechnol.* **2014**, 9 (4), 262—267.
- (4) He, Y.-M.; Clark, G.; Schaibley, J. R.; He, Y.; Chen, M.-C.; Wei, Y.-J.; Ding, X.; Zhang, Q.; Yao, W.; Xu, X.; et al. Single Quantum Emitters in Monolayer Semiconductors. *Nature Nanotechnol.* **2015**, *10* (6), 497–502.
- (5) Koperski, M.; Nogajewski, K.; Arora, A.; Cherkez, V.; Mallet, P.; Veuillen, J.-Y.; Marcus, J.; Kossacki, P.; Potemski, M. Single Photon Emitters in Exfoliated WSe 2 Structures. *Nature Nanotechnol.* **2015**, 10 (6), 503–506.
- (6) Zuo, X.; Zhang, H.; Zhu, Q.; Wang, W.; Feng, J.; Chen, X. A Dual-Color Fluorescent Biosensing Platform Based on WS2 Nanosheet for Detection of Hg2+ and Ag. *Biosens. Bioelectron.* **2016**, *85*, 464–470.
- (7) Kuru, C.; Choi, D.; Kargar, A.; Liu, C. H.; Yavuz, S.; Choi, C.; Jin, S.; Bandaru, P. R. High-Performance Flexible Hydrogen Sensor Made of WS2 Nanosheet—Pd Nanoparticle Composite Film. *Nanotechnology* **2016**, *27* (19), 195501.
- (8) Pospischil, A.; Furchi, M. M.; Mueller, T. Solar-Energy Conversion and Light Emission in an Atomic Monolayer p—n Diode. *Nature Nanotechnol.* **2014**, *9* (4), 257–261.
- (9) Mak, K. F.; Lee, C.; Hone, J.; Shan, J.; Heinz, T. F. Atomically Thin MoS 2: A New Direct-Gap Semiconductor. *Physical review letters* **2010**, *105* (13), 136805.
- (10) Splendiani, A.; Sun, L.; Zhang, Y.; Li, T.; Kim, J.; Chim, C.-Y.; Galli, G.; Wang, F. Emerging Photoluminescence in Monolayer MoS2. *Nano Lett.* **2010**, *10* (4), 1271–1275.
- (11) Ross, J. S.; Wu, S.; Yu, H.; Ghimire, N. J.; Jones, A. M.; Aivazian, G.; Yan, J.; Mandrus, D. G.; Xiao, D.; Yao, W.; et al. Electrical Control of Neutral and Charged Excitons in a Monolayer Semiconductor. *Nat. Commun.* **2013**, *4* (1), 1–6.
- (12) Tongay, S.; Zhou, J.; Ataca, C.; Lo, K.; Matthews, T. S.; Li, J.; Grossman, J. C.; Wu, J. Thermally Driven Crossover from Indirect toward Direct Bandgap in 2D Semiconductors: MoSe2 versus MoS2. *Nano Lett.* **2012**, *12* (11), 5576–5580.
- (13) Niehues, I.; Schmidt, R.; Druppel, M.; Marauhn, P.; Christiansen, D.; Selig, M.; Berghäuser, G.; Wigger, D.; Schneider, R.; Braasch, L.; et al. Strain Control of Exciton—Phonon Coupling in Atomically Thin Semiconductors. *Nano Lett.* **2018**, *18* (3), 1751—1757.

- (14) Roldán, R.; Castellanos-Gomez, A.; Cappelluti, E.; Guinea, F. Strain Engineering in Semiconducting Two-Dimensional Crystals. *J. Phys.: Condens. Matter* **2015**, 27 (31), 313201.
- (15) Castellanos-Gomez, A.; Roldán, R.; Cappelluti, E.; Buscema, M.; Guinea, F.; van der Zant, H. S.; Steele, G. A. Local Strain Engineering in Atomically Thin MoS2. *Nano Lett.* **2013**, *13* (11), 5361–5366.
- (16) Liu, Z.; Amani, M.; Najmaei, S.; Xu, Q.; Zou, X.; Zhou, W.; Yu, T.; Qiu, C.; Birdwell, A. G.; Crowne, F. J.; et al. Strain and Structure Heterogeneity in MoS 2 Atomic Layers Grown by Chemical Vapour Deposition. *Nat. Commun.* **2014**, *5* (1), 1–9.
- (17) Li, B.; Gong, Y.; Hu, Z.; Brunetto, G.; Yang, Y.; Ye, G.; Zhang, Z.; Lei, S.; Jin, Z.; Bianco, E.; et al. Solid-Vapor Reaction Growth of Transition-Metal Dichalcogenide Monolayers. *Angew. Chem.* **2016**, 128 (36), 10814–10819.
- (18) Baldo, M.; Stojanović, V. Excitonic Interconnects. *Nat. Photonics* **2009**, 3 (10), 558-560.
- (19) Mak, K. F.; He, K.; Shan, J.; Heinz, T. F. Control of Valley Polarization in Monolayer MoS 2 by Optical Helicity. *Nature Nanotechnol.* **2012**, *7* (8), 494–498.
- (20) Bao, W.; Borys, N. J.; Ko, C.; Suh, J.; Fan, W.; Thron, A.; Zhang, Y.; Buyanin, A.; Zhang, J.; Cabrini, S.; et al. Visualizing Nanoscale Excitonic Relaxation Properties of Disordered Edges and Grain Boundaries in Monolayer Molybdenum Disulfide. *Nat. Commun.* **2015**, *6* (1), 1–7.
- (21) Park, K.-D.; Khatib, O.; Kravtsov, V.; Clark, G.; Xu, X.; Raschke, M. B. Hybrid Tip-Enhanced Nanospectroscopy and Nanoimaging of Monolayer WSe2 with Local Strain Control. *Nano Lett.* **2016**, *16* (4), 2621–2627.
- (22) Su, W.; Kumar, N.; Dai, N.; Roy, D. Nanoscale Mapping of Intrinsic Defects in Single-Layer Graphene Using Tip-Enhanced Raman Spectroscopy. *Chem. Commun.* **2016**, 52 (53), 8227–8230.
- (23) Zhang, Y.; Voronine, D. V.; Qiu, S.; Sinyukov, A. M.; Hamilton, M.; Liege, Z.; Sokolov, A. V.; Zhang, Z.; Scully, M. O. Improving Resolution in Quantum Subnanometre-Gap Tip-Enhanced Raman Nanoimaging. *Sci. Rep.* **2016**, *6* (1), 1–9.
- (24) Voronine, D. V.; Lu, G.; Zhu, D.; Krayev, A. Tip-Enhanced Raman Scattering of MoS 2. *IEEE J. Sel. Top. Quantum Electron.* **2017**, 23 (1), 138–143.
- (25) Lee, Y.; Yun, S. J.; Kim, Y.; Kim, M. S.; Han, G. H.; Sood, A. K.; Kim, J. Near-Field Spectral Mapping of Individual Exciton Complexes of Monolayer WS 2 Correlated with Local Defects and Charge Population. *Nanoscale* **2017**, *9* (6), 2272–2278.
- (26) Darlington, T. P.; Krayev, A.; Venkatesh, V.; Saxena, R.; Kysar, J. W.; Borys, N. J.; Jariwala, D.; Schuck, P. J. Facile and Quantitative Estimation of Strain in Nanobubbles with Arbitrary Symmetry in 2D Semiconductors Verified Using Hyperspectral Nano-Optical Imaging. *J. Chem. Phys.* **2020**, *153* (2), 024702.
- (27) Ambardar, S.; Kamh, R.; Withers, Z.; Sahoo, P.; Voronine, D. V. Coupling Nanobubbles in 2D Lateral Heterostructures. *Nanoscale* **2022**, *14*, 8050–8059.
- (28) Gupta, S.; Johnston, A.; Khondaker, S. Optoelectronic Properties of MoS2/Graphene Heterostructures Prepared by Dry Transfer for Light-Induced Energy Applications. *J. Electron. Mater.* **2022**, 1–13.
- (29) Moore, D.; Jo, K.; Nguyen, C.; Lou, J.; Muratore, C.; Jariwala, D.; Glavin, N. R. Uncovering Topographically Hidden Features in 2D MoSe2 with Correlated Potential and Optical Nanoprobes. *npj 2D Materials and Applications* **2020**, 4 (1), 1–7.
- (30) Chowdhury, T.; Jo, K.; Anantharaman, S. B.; Brintlinger, T. H.; Jariwala, D.; Kempa, T. J. Anomalous Room-Temperature Photoluminescence from Nanostrained MoSe2Monolayers. *ACS Photonics* **2021**, *8* (8), 2220–2226.
- (31) Okuno, Y.; Lancry, O.; Tempez, A.; Cairone, C.; Bosi, M.; Fabbri, F.; Chaigneau, M. Probing the Nanoscale Light Emission Properties of a CVD-Grown MoS 2 Monolayer by Tip-Enhanced Photoluminescence. *Nanoscale* **2018**, *10* (29), 14055–14059.
- (32) Xue, W.; Sahoo, P. K.; Liu, J.; Zong, H.; Lai, X.; Ambardar, S.; Voronine, D. V. Nano-Optical Imaging of Monolayer MoSe2-WSe2

- Lateral Heterostructure with Subwavelength Domains. Journal of Vacuum Science & Technology A: Vacuum, Surfaces, and Films 2018, 36 (5), 05G502.
- (33) Albagami, A.; Ambardar, S.; Hrim, H.; Sahoo, P. K.; Emirov, Y.; Gutiérrez, H. R.; Voronine, D. V. Tip-Enhanced Photoluminescence of Freestanding Lateral Heterobubbles. *ACS Appl. Mater. Interfaces* **2022**, *14* (8), 11006–11015.
- (34) Wang, C.-F.; Zamkov, M.; El-Khoury, P. Z. Ambient Tip-Enhanced Photoluminescence with 5 Nm Spatial Resolution. *J. Phys. Chem. C* **2021**, *125* (22), 12251–12255.
- (35) Sahoo, P. K.; Zong, H.; Liu, J.; Xue, W.; Lai, X.; Gutiérrez, H. R.; Voronine, D. V. Probing Nano-Heterogeneity and Aging Effects in Lateral 2D Heterostructures Using Tip-Enhanced Photoluminescence. *Optical Materials Express* **2019**, 9 (4), 1620–1631.
- (36) Novotny, L.; Bian, R. X.; Xie, X. S. Theory of Nanometric Optical Tweezers. *Phys. Rev. Lett.* **1997**, 79 (4), 645.
- (37) Roth, R. M.; Panoiu, N. C.; Adams, M. M.; Osgood, R. M.; Neacsu, C. C.; Raschke, M. B. Resonant-Plasmon Field Enhancement from Asymmetrically Illuminated Conical Metallic-Probe Tips. *Opt. Express* **2006**, *14* (7), 2921–2931.
- (38) Demming, A. L.; Festy, F.; Richards, D. Plasmon Resonances on Metal Tips: Understanding Tip-Enhanced Raman Scattering. *J. Chem. Phys.* **2005**, *122* (18), 184716.
- (39) Luo, S.; Cullen, C. P.; Guo, G.; Zhong, J.; Duesberg, G. S. Investigation of Growth-Induced Strain in Monolayer MoS2 Grown by Chemical Vapor Deposition. *Appl. Surf. Sci.* **2020**, *508*, 145126.
- (40) Van Der Zande, A. M.; Huang, P. Y.; Chenet, D. A.; Berkelbach, T. C.; You, Y.; Lee, G.-H.; Heinz, T. F.; Reichman, D. R.; Muller, D. A.; Hone, J. C. Grains and Grain Boundaries in Highly Crystalline Monolayer Molybdenum Disulphide. *Nature materials* **2013**, *12* (6), 554–561.
- (41) Krustok, J.; Raadik, T.; Jaaniso, R.; Kiisk, V.; Sildos, I.; Marandi, M.; Komsa, H.-P.; Li, B.; Zhang, X.; Gong, Y.; et al. Optical Study of Local Strain Related Disordering in CVD-Grown MoSe2Monolayers. *Appl. Phys. Lett.* **2016**, *109* (25), 253106.
- (42) Sevik, C. Assessment on Lattice Thermal Properties of Two-Dimensional Honeycomb Structures: Graphene, h-BN, h-MoS 2, and h-MoSe 2. *Phys. Rev. B* **2014**, *89* (3), 035422.
- (43) El-Mahalawy, S. H.; Evans, B. L. The Thermal Expansion of 2H-MoS2, 2H-MoSe2 and 2H-WSe2 between 20 and 800 C. *J. Appl. Crystallogr.* **1976**, 9 (5), 403–406.